Journal of Materials Chemistry A

ROYAL SOCIETY OF CHEMISTRY

PAPER

View Article Online
View Journal | View Issue

Cite this: J. Mater. Chem. A, 2025, 13, 1372

Advancing high capacity 3D VO_2(B) cathodes for improved zinc-ion battery performance†

Iman P. Pinnock, [a] Yujia Fan,[a] Yijia Zhu,[a] Bastola Narayan,[b] Tianlei Wang,[c] Ivan P. Parkin *[c] and Buddha Deka Boruah *[a]

Aqueous zinc-ion batteries (AZIBs) have gained attention for their intrinsic characteristics, driven by key advantages, such as cost-effectiveness, widespread availability of zinc, and reduced environmental impact, making AZIBs a promising alternative to lithium-based batteries, with potential applications in mini-grid and mini off-grid energy systems. However, achieving high capacity is crucial for AZIBs, driving the research focus towards developing advanced cathode materials. Vanadium dioxide (VO_2(B)) has emerged as a promising cathode material for AZIBs, owing to its large tunnel-like framework that accommodates Zn^{2+} ions for enhanced capacity. The overall performance of cathode materials depends not only on their inherent properties but also on their synthesis methods, electrode processing techniques, and achievement of ultra-high mass loading for 3D electrodes. In this study, we explore the optimization of VO_2(B) cathodes through refined synthesis approaches, various electrode processing methods, and the development of 3D electrodes with ultrahigh mass loading. As a result, we achieved significant improvements in specific capacity, from 310 mA h g^{-1} to 500 mA h g^{-1}, through parameter tuning. Additionally, our optimized cathodes demonstrated a stable capacity retention of 71.5% after 1000 cycles. We also developed ultra-high mass loading cathodes of 24 g cm^{-2}, achieving an areal capacity of 4.6 mA h cm^{-2}, with a stability of 81.5% after 1000 cycles. This work provides a comprehensive approach to obtaining high-capacity cathodes, contributing to the advancement of reliable and high-performance AZIBs.

Received 14th September 2024
Accepted 21st November 2024

DOI: 10.1039/d4ta06572g

rsc.li/materials-a

Introduction

The growing reliance on energy storage systems has rapidly increased, pushed by the need for decarbonisation and the efficient utilisation of green energy sources, such as solar and wind power. Among various energy storage technologies, lithium-ion systems have played a pivotal role, especially in batteries, offering the required energy storage performance owing to their high energy density and lightweight characteristics. However, growing concerns are there regarding specific applications, particularly in mini-grid and mini off-grid energy storage, in which cost-effectiveness, environmental safety, and sustainability are the priorities. Li-ion batteries possess safety issues, high costs and limited resource availability, which, alongside the use of potentially flammable electrolytes, render them unsuitable for mini-grid and mini off-grid storage systems. One emerging alternative which has attracted attention are aqueous zinc-ion batteries (AZIBs), in response to this new demand for superior batteries. AZIBs have become a focal point of interest in the field of electrochemical energy storage due to several advantages, including the ease of manufacturing; AZIBs can be assembled in open air,[1] whereas lithium-ion batteries (and sodium ion batteries) require specialised controlled conditions, thus eliminating extra costs. Zinc itself is also more cost-effective due to its high natural abundance, which is four times that of lithium, resulting in the cost of zinc ($0.5–$1.5/lb) being significantly lower than that of lithium ($8–$11/lb). Zinc's abundancy in the earth's crust is 79 ppm, ranking it the fourth place in the world metal production, and making it a strong contender when considering resource availability, cost, and sustainability.[2] The electrolytes used by AZIBs are more environmentally friendly, as they are mainly aqueous (if not, slightly acidic)[3] and affordable. Zinc anodes offer a high gravimetric capacity (820 mA h g^{-1}) and volumetric capacity (5855 mA h cm^{-3}),[2,4–6] along with a low redox potential (−0.762 V *vs.* SHE). These properties make them well-suited for use in aqueous electrolytes, and the two-electron transfer process during redox reactions enables high-energy density in AZIBs.[1,2] Moreover, multivalent zinc ions can transfer two electrons which accelerates more energy storage than univalent batteries.[7] The ionic radius of the zinc ion (0.74 Å) is

[a]Institute for Materials Discovery (IMD), University College London (UCL), London WC1E 7JE, UK. E-mail: b.boruah@ucl.ac.uk

[b]Department of Mechanical Engineering, University of Bath, Bath, BA2 7AY, UK

[c]Department of Chemistry, University College London (UCL), London WC1H 0AJ, UK. E-mail: i.p.parkin@ucl.ac.uk

† Electronic supplementary information (ESI) available. See DOI: https://doi.org/10.1039/d4ta06572g

similar to that of lithium (0.69 Å), relative to the radius of other alternatives, such as sodium, which has a radius of 1.02 Å. Thus, it can be seen clearly that AZIBs are a promising alternative to lithium-ion batteries, and suitable for mini-grid and mini off-grid storage systems. However, there are currently many issues faced by AZIBs, such as zinc dendrite growth in aqueous electrolytes,[8] side reactions,[9] and cathode dissolution.[10]

Cathode material in AZIBs is of high importance due to the requirement of a suitable material that can facilitate the high polarisation of bivalent zinc ions,[11] thus requiring the material to possess high capacity and the appropriate structural stability to facilitate (de)intercalation of ions,[1] making manganese and vanadium-based materials, organic compounds, and Prussian blue analogues most promising candidates.[11] Manganese-based cathodes have been considered due to their high theoretical capacity (309 mA h g^{-1}),[2] low cost and toxicity, environmentally friendliness and multivalent states.[12] However, severe capacity fading is known to occur due to the dissolution of manganese into the electrolyte with cycling. Polyvalent manganese oxides have multiple crystal structures,[13] which provide frameworks to accommodate various cations.[12] Organic materials possess abundant chemical composition, biodegradability, affordability, multiple electron reactions and a flexible electrochemical window.[11] Currently, there is limited research into organic materials for cathode use. However, the results produced so far show a theoretical capacity of 335 mA h g^{-1},[14] which is similar to that of manganese-based materials. Prussian blue analogues have an open framework structure[5,12] with a face-centred cubic lattice, thus resulting in large ion-intercalation sites.[11] The material displays a decent cycle performance (81% retention after 100 cycles),[2] but research has shown them to yield a lower specific capacity than the other materials (55.6 mA h g^{-1}, 120 mA h g^{-1} and 100 mA h g^{-1}).[2,5,11] Although the large interstitial sites and large tunnels allow easy and reversible electrochemical insertion/extraction of Zn^{2+} ions,[15] the low theoretical specific capacity and relatively low cycle performance make it unattractive.

Conversely, vanadium-based materials (namely, vanadium oxides) are of great interest due to their large-tunnel framework structure, presenting the potential possibility to accommodate numerous Zn^{2+} ions for storage. Vanadium pentoxide (V_2O_5) has a structure where the lattice contains covalent bonds, weak van der Waals forces and hydrogen bonds, allowing Zn^{2+} to attach and detach freely, resulting in excellent rate performance.[11] However, it suffers from instability and low capacity when subjected to repeated intercalation of ions because of the unstable single layer structure and pure +5 valence.[16,17] In comparison, VO_2 has a tunnel-like framework, which results in a remarkable ability for rapid Zn^{2+} (de)intercalation, displaying outstanding rate performance.[18] VO_2 has numerous polymorphs with different complex crystal frameworks.[12] However, VO_2(B) stands out on account of its distinct structure that comprises distorted VO_6 octahedra connected through edge sharing, which is able to withstand (de)intercalation of Zn^{2+} ions.[2] It should be noted that the overall performance of cathode materials depends not only on their inherent properties but also on their synthesis methods, electrode processing techniques, and achievement of ultra-high mass loading. Hence, there is a need for sequential studies to establish standard electrode processing techniques, with the goal of achieving maximum capacities during testing and approaching the theoretical values.

In this study, we investigate sequential synthesis methods and processing techniques for electrode materials to enhance the capacities of VO_2(B) as a cathode material. This is followed by further efforts to achieve ultra-high mass loading for attaining ultrahigh-areal capacities compared to conventional counterparts. Our research aims to demonstrate how the capacity of active materials can be improved through advanced synthesis and processing techniques of battery electrodes, thereby contributing to the development of reliable and high-performance AZIBs.

Results and discussion

Effective mass utilisation on the cathode without losing electrode conductivity and capacity is essential for achieving high performance. Fig. 1a and b show the schematics of coin cells with conventional slurry-casted cathodes on flat current collectors with an approximate thickness of 0.05 mm, while the 3D ultrathick electrodes have an approximate thickness of 2.55 mm, including the carbon paper and vitreous carbon foam. Digital images of the developed ultrathick electrodes are shown in Fig. 1c, obtained by processing the optimized VO_2(B) cathode materials onto a 3D vitreous carbon foam. This 3D vitreous carbon foam framework offers advantages such as rapid Zn^{2+} ion diffusion without losing conductivity over the 3D scaffolds (Fig. 1d), leading to superior charge storage capacities compared to conventional electrodes when normalized by area. Additionally, VO_2(B) has a tunnel-like framework (Fig. 1e) that facilitates effective Zn^{2+} ion diffusion through tunnels in the *b*-direction and *c*-direction, resulting in extremely high capacities. Fig. 1f shows low-magnification SEM images of the 3D cathode, while the high-magnification images (Fig. 1g and h) demonstrate the decoration of VO_2(B) nanorods on the 3D current collector scaffolds.

Synthesis methods

It should be noted that the capacity of the VO_2(B) material depends not only on the electrode processing, but also on the synthesis process. To obtain optimum capacities of VO_2(B), we explored both conventional hydrothermal synthesis and a rapid multiwave reaction process. The specific synthesis conditions are described in detail in the Experimental section (ESI†). Fig. 2a shows the SEM image of VO_2(B) obtained using the multiwave reaction process, where multiwave digestion produced nanorods alongside clusters. The TEM image in Fig. 2b further supports this observation. From the HRTEM image in Fig. 2c, a calculated *d*-spacing value of 0.265 nm was obtained, corresponding to the (−3 1 1) planes in the monoclinic structure of VO_2(B). In contrast, the hydrothermal synthesis produced uniform nanorod morphologies, as shown in Fig. 2d and e, with a calculated *d*-spacing value of 0.351 nm

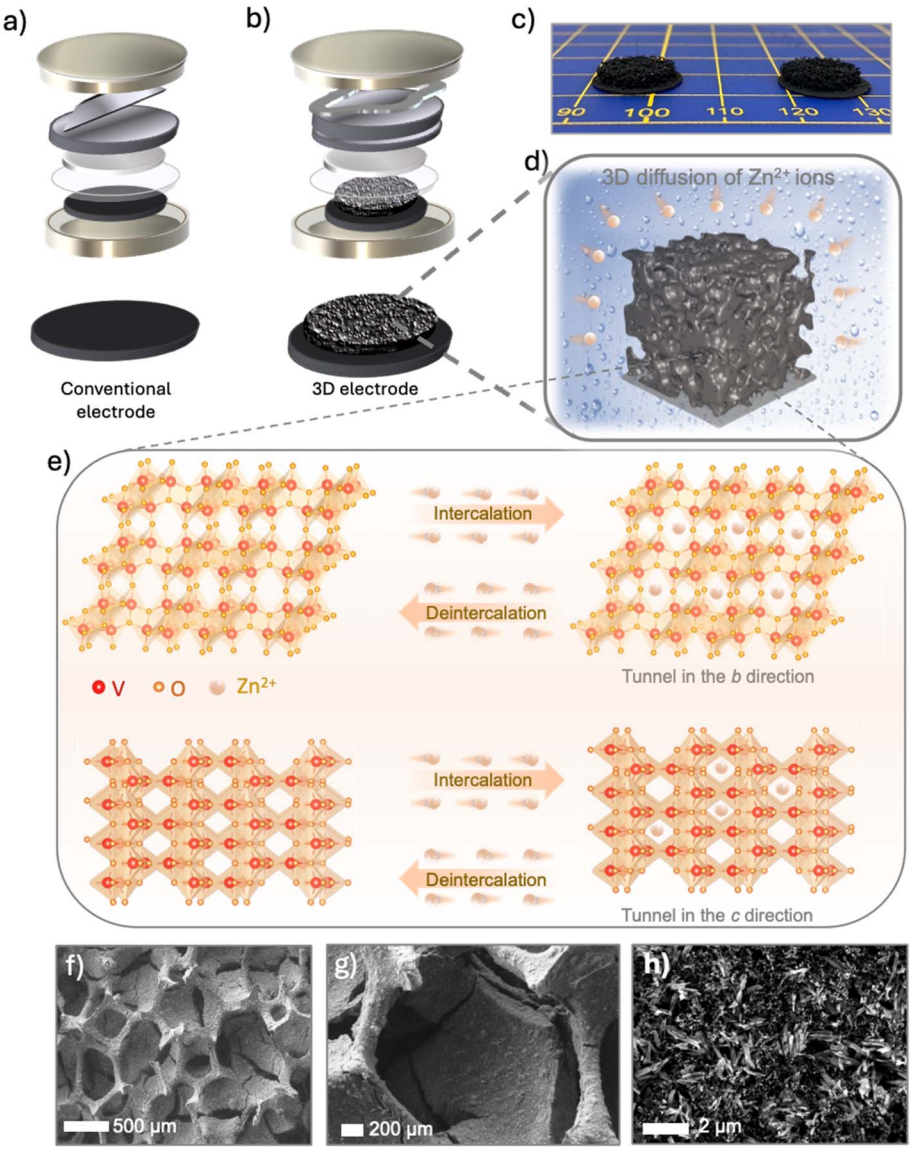

Fig. 1 Schematic of AZIB with (a) a conventional, slurry-casted electrode and (b) a 3D, ultrathick electrode. (c) Picture of the 3D electrodes assembled with the vitreous carbon foam and attached to carbon paper, and (d) zoomed-in schematic of the 3D cathode. (e) Schematic of the Zn^{2+} (de)intercalation VO_2(B) nanorods projected along the *b*- and *c*-directions. (f–h) SEM images of the 3D cathode at increasing magnifications.

corresponding to the (1 1 0) planes (Fig. 2f) in the monoclinic structure of VO_2(B). These *d*-spacings match that of the XRD spectra, and both planes produce strong peaks in the spectra. The obtained XRD spectra (Fig. 2g) display identical patterns for both methods, with the corresponding planes indicated. From the MDI Jade XRD database, the correct peaks for VO_2(B) are displayed. These include the strong peaks at $2\theta = 14.4°$, 15.4°, 25.2°, 29.0°, 30.1°, 44.1°, 44.9° and 49.2°, which correspond to the (001), (200), (110), (002), (−401), (003), (−601) and (020) Miller indices, respectively.[19] The correct phase was obtained, especially *via* hydrothermal synthesis, as every peak with an intensity above 5 is displayed. Furthermore, the two peaks at 14° and 15° (approx.) are visible, which are not shown in the other phases of VO_2(B).[20] Additionally, the XRD results demonstrate that V_2O_5 has not been produced. Although the XRD spectra are similar, VO_2(B) exhibits the highest intensity in the (110) peak, whereas V_2O_5 shows the highest intensity in the (001) peak.[21] The hydrothermally synthesised VO_2(B) exhibits sharper peaks than the multiwave-reacted VO_2(B), indicating a higher degree of crystallinity.[22,23]

To further ensure the VO_2(B) material was as expected, Raman spectra of the materials were obtained (Fig. 2h), from which all the expected Raman peaks were visible in the spectra for both samples.[24,25] The peaks at 139 cm^{-1} and 191 cm^{-1} represent the layered lattice structure. The peaks at 282 cm^{-1} and 404/406 cm^{-1} represent the V=O bending vibration bonds, while the peak at 668 cm^{-1} represents the V–O–V stretching mode, resulting from the corner-shared oxygens of two

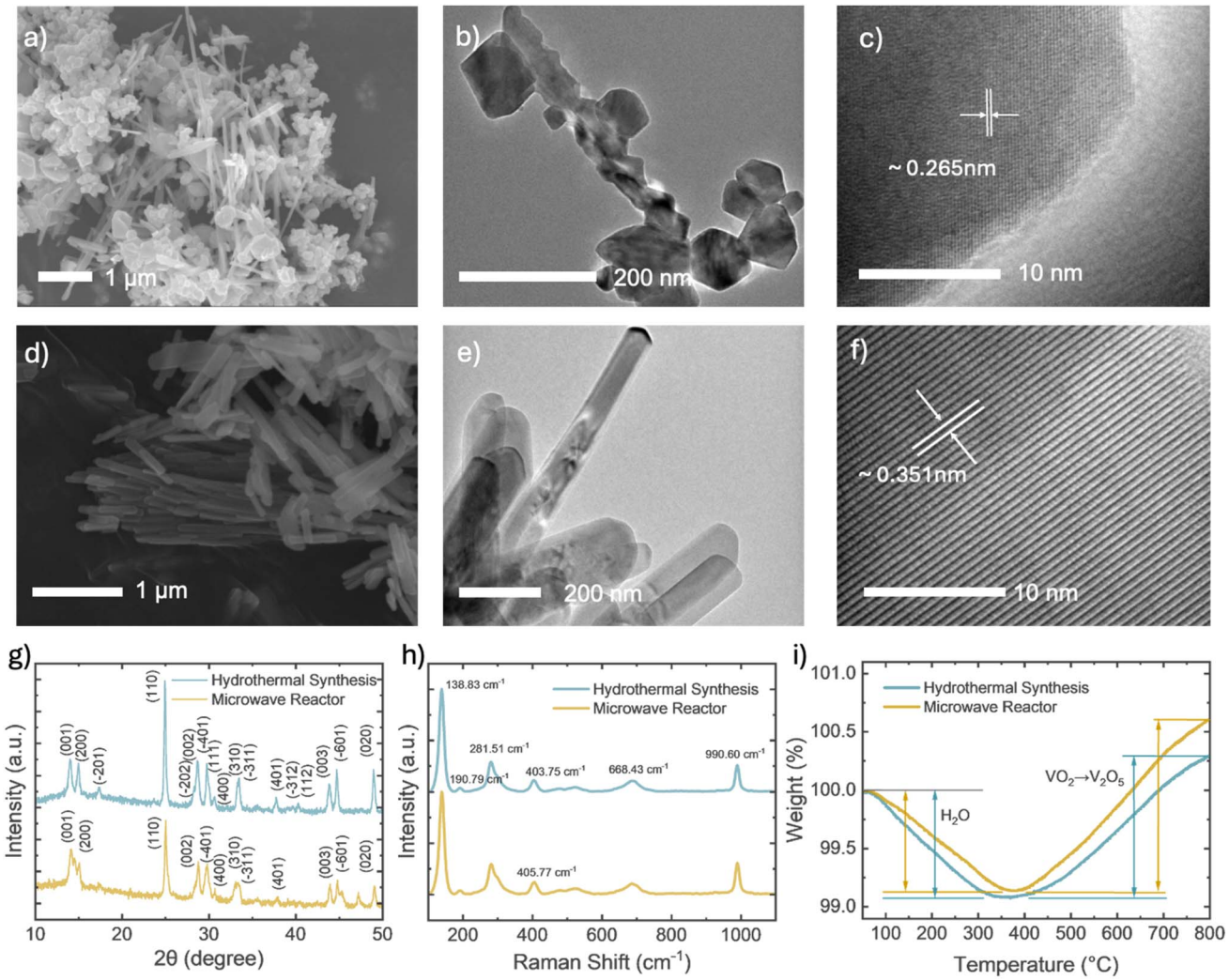

Fig. 2 SEM, TEM and HRTEM images of (a–c) multiwave digested and (d–f) hydrothermal synthesised VO_2(B). TEM and HRTEM images of (b and c) multiwave digested and (e and f) hydrothermal synthesised VO_2(B). (g) XRD, (h) Raman spectra and (i) TGA profiles of the two VO_2(B) samples.

pyramids. The peak at 990.60 cm^{-1} represents the terminal oxygen (V=O) stretching vibration.[24] The presence of water molecules in the two differently synthesised VO_2(B) samples was investigated by TGA analysis under nitrogen flow, as depicted in Fig. 2i. Both samples exhibit a mass loss up to approx. 375 °C (0.9 wt% for multiwave VO_2(B) and 1 wt% for hydrothermal VO_2(B)). The weak weight loss (<1%) suggested that there was no lattice water that could have been present originally during the stabilisation of the VO_2(B) intermediate structure. Additionally, as the weight was very nearly constant, it indicated that VO_2(B) can be stable in the N_2 atmosphere.[26,27]

XPS analysis was conducted to further confirm the transformation of the oxidation number of vanadium, alongside identifying which sample had more oxygen vacancies. Fig. 3 displays the XPS spectra of the two samples. Fig. 3a and c show that the binding energy is at EB ($V_{3/2p}$) = 517.8 eV and 517.9 eV, respectively. These peak positions correspond to the V^{5+} cations. By comparison, V^{4+} cations correspond to the binding energies of 516.7 and 524.3 eV.[28,29] The ratio between the peak area of V^{4+}/V^{5+} for the multiwave digested sample is 6.56. For the hydrothermally synthesised sample, the ratio is 7.33, confirming a higher concentration of V^{4+} in the hydrothermally synthesised VO_2(B) (which indicated that more of the reactants changed from V_2O_5 to VO_2). However, it is a very small discrepancy. In Fig. 3b and d, the oxygen component can be observed. The peaks at 530.5 eV and 530.4 eV correspond to the lattice oxygen, and the smaller peaks at 531.6 eV and 531.7 eV (respectively) represent the oxygen absorbed.[30,31] The area of the V–OH peak for the multiwave VO_2(B) is 13 767.6, which is larger than that of the hydrothermal VO_2(B) (12 982.2). This suggests that the hydrothermally synthesised VO_2(B) has a lower oxygen concentration (more oxygen vacancies), resulting in more efficient (de)intercalation of Zn^{2+} ions. BET analysis was performed to investigate which synthesis method produced VO_2(B) with a larger surface area. Fig. S1† displays the N_2 adsorption and desorption isotherms of the VO_2(B) samples synthesised hydrothermally and multiwave reacted. The curves suggest that both samples exhibit type III isotherms. This is expected as both

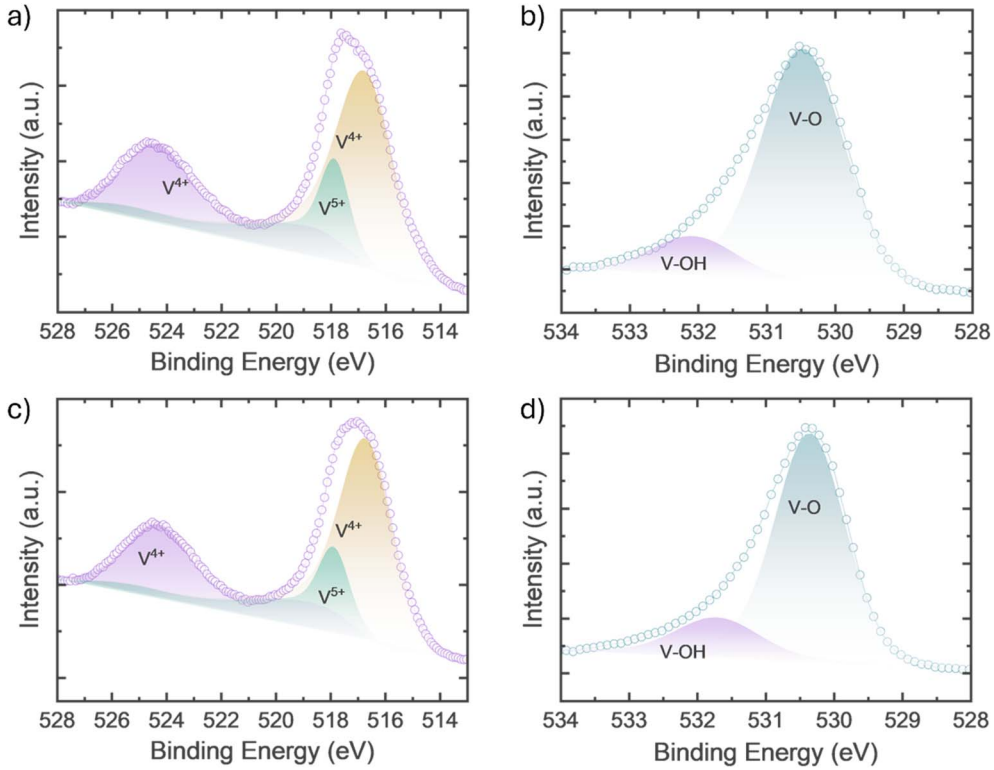

Fig. 3 XPS spectra of (a and b) multiwave digested and (c and d) hydrothermally synthesised VO_2(B) – (a and c) V 2p and (b and d) O 1s.

are VO_2(B), indicating that the *c* value (BET constant) is less than 1 due to the type of isotherm. The BET constant relates to the adsorption energy of the first monolayer – as it is less than 1, it shows the formation of a multilayer with no monolayer as there is no asymptote in the curve.[32,33] Additionally, surface area tests were performed on the samples, which showed that the measured specific surface areas were 23.88 $m^2\ g^{-1}$ for the multiwave sample and 24.49 $m^2\ g^{-1}$ for the hydrothermal sample. This confirmed that there was no significant difference in the surface areas between the two samples, which was further supported by the lack of any significant difference between the absorbed volume (the hydrothermally synthesised VO_2(B) absorbed a slightly larger volume of approx. 5 $cm^3\ g^{-1}$ more).

Next, the electrochemical performance of the two samples was evaluated in coin cells using a conventional electrode configuration, as described in the Experimental section (ESI†). Comparative cyclic voltammetry (CV) and galvanostatic charge–discharge (GCD) measurements were taken of cells assembled with hydrothermal and multiwave synthesised VO_2(B) cathodes. Initially, a conventional mass loading was employed and was kept relatively the same to allow for uniformity in comparison between the samples. CVs were measured at different scan rates (0.2–1.0 mV s^{-1}) and in a specific voltage window (0.2–1.6 V). In Fig. 4a and b, the CVs display two cathodic and two anodic peaks, corresponding to the intercalation and deintercalation reactions. Two anodic peaks can be seen at approximately 0.7 V and 1.1 V, and the cathodic peaks are positioned at approx. 0.5 V and 0.9 V. The two peaks indicate two different Zn^+ insertion/extraction processes, thus confirming the redox reaction of VO_2(B) during discharge/charge.[34] Eqn (1) and (2) describe the electrochemical reaction of the Zn/VO_2 battery, with eqn (1) being the cathode and eqn (2) the anode.[35]

$$VO_2(B) + xZn^{2+} + 2xe^- \leftrightarrow Zn_xVO_2(B) \quad (1)$$

$$Zn \leftrightarrow Zn^{2+} + 2e^- \quad (2)$$

Alongside the H^+ ion intercalation, (de)doping processes may take place. When the cathode is discharged, H^+ ions from the electrolyte diffuse into the VO_2(B) structure, which is known as H^+ insertion. Dedoping is the release of H^+ back into the electrolyte when charged.[36] The obtained CV curves indicated that the cathodes made with hydrothermally synthesised VO_2 exhibit sharper peaks, with two clear peaks for each Zn^+ process, and an overall slightly higher specific capacity. Due to the sharp peaks, the potential difference (peak separation) is smaller, indicating a highly reversible redox reaction and efficient charge storage processes. *Ex situ* charge/discharge tests on the cells were run to different voltages, as seen in Fig. S2a,† which was followed by Raman measurements. When the AZIB discharges, Zn^{2+} ions from the anode are stripped and then intercalated into the cathode. Therefore, the cathode material (VO_2(B)) is being reduced, changing from V^{4+} to V^{3+}. It is likely that VO_2(B) has undergone a phase transition from a monoclinic to tetragonal structure when discharged. This phase transition involves significant rearrangement of atoms, and changes in the bond length and angles. When the cell is

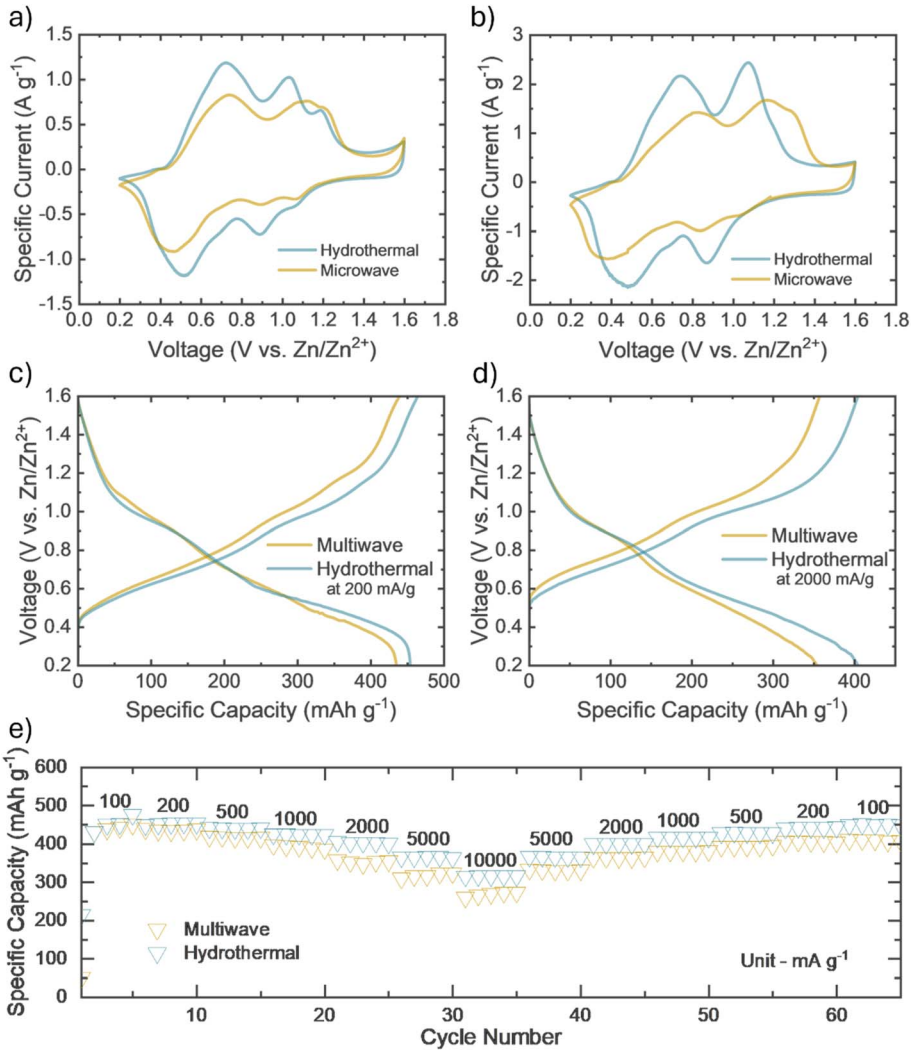

Fig. 4 Comparative CV curves of AZIBs at scan rates of (a) 0.5 mV s^{-1} and (b) 1.0 mV s^{-1}. GDCs curves at specific currents of (c) 200 mA g^{-1} and (d) 2000 mA g^{-1}. (e) Rate capacity tests for AZIBs, with cathodes synthesised *via* hydrothermal and multiwave synthesis approaches.

discharged to 0.2 V, a peak appears at approx. 800–1000 cm^{-1}. This could be due to the carboxylic acid dimer forming, alongside C–C aliphatic chains and C–O–C bonds forming.[37,38] Another broad peak appears at approx. 500 cm^{-1}, which is seen in the VO_2(A) phase. This is due to its tetragonal structure that is not visible in the VO_2(B) spectra, which further supports the theory that VO_2(B) undergoes a phase transition when discharged fully.[37,39] When the cell is charged, the cathode is oxidised, returning the vanadium to its usual oxidation state of +4 as a result of the Zn^{2+} ions deintercalating and returning to the electrolyte.[40]

GCD measurements were taken at different specific currents, ranging from 100 to 10 000 mA g^{-1}, to evaluate the electrochemical performance of the materials. It was observed that the specific capacities of the hydrothermally synthesised VO_2(B) samples are greater than those of the multiwave digested samples, which is in agreement with the CV results. For example, the multiwave-treated sample exhibits specific capacities of 435 mA h g^{-1} and 353 mA h g^{-1} at specific currents of 200 mA g^{-1} and 20 000 mA g^{-1}, respectively. These capacities increase to 454 mA h g^{-1} and 404 mA h g^{-1} for the hydrothermally synthesised VO_2(B), as shown in Fig. 4c and d, which is consistent with the trends indicated by the CV graphs. Moreover, Fig. 4e illustrates a comparison of the rate capacity tests, showing that the cell with the hydrothermal VO_2(B) cathode achieved higher specific capacities across all tested specific currents, whether low or high. This suggests that the overall electrochemical performance is better. This is likely due to the increase in the number of oxygen vacancies and higher concentration of V^{4+} in the hydrothermal samples, which could enable more efficient intercalation of Zn^{2+} ions compared to the multiwave reactor samples. Additionally, we conducted long-term cycling tests on the coin cells to assess their stability, applying a specific current of 1000 and 2000 mA g^{-1}. Both cells performed reliably for 500 cycles, but the hydrothermally synthesised VO_2(B) cathode exhibited a higher specific capacity (346 mA h g^{-1}) compared to the multiwave-reacted VO_2(B) cathode (261 mA h g^{-1}), as shown in Fig. S3.† Both cells exhibited a slight decrease in specific capacity over time, with the hydrothermal cell undergoing an activation period that is

likely due to further material activation during cycling. However, based on the data and methods presented, the hydrothermally synthesised VO_2(B) was determined to be the optimal material. Consequently, the hydrothermal method was exclusively employed from this point onward.

Drying methods

The identified optimal hydrothermal synthesis method was further developed, achieving relatively higher mass loading (~4.0 mg cm^{-2}). Additionally, the study aimed to understand how different electrode drying processes (freeze-drying and conventional oven drying) influence charge storage performance. The CV curves at different scan rates of the oven and freeze-dried cells can be seen in Fig. 5a and b. In Fig. 5c and d, for high mass loading (~4.0 mg cm^{-2}), the freeze-dried cathode significantly outperforms the oven-dried one, which indicated that the porosity of the material was increased *via* freeze-drying (see further). The freeze-dried cathode yields a specific current at each peak that is larger than that of the oven-dried sample, as they are also greater in magnitude. Fig. S4† displays the CV curves of the low mass loading cathodes (~1.5 mg cm^{-2}). The freeze-dried cathode still exhibited the best performance, with the discrepancy between the obtained specific currents increasing as the scan rates increased. For each mass loading, the freeze-dried cathodes performed the best, yielding higher specific currents and sharper peaks, indicating the two intercalation processes. This supports the theory that the freeze-dried electrode has increased porosity, and thus increases the surface area, resulting in greater movement of ions (see further).

Assuming the peak current (i) obeys a power law relationship with the scan rate (v), they can be defined as follows:

$$i = av^b \tag{3}$$

$$\Rightarrow \log(i) = \log(a) + b \times \log(v) \tag{4}$$

where a and b are variable parameters.[41,42]

Eqn (4) can be viewed as the equation for a linear relationship. If the b value ≈ 0.5, the electrochemical process is diffusion-controlled. Conversely, if the b value ≈ 1.0, it indicates

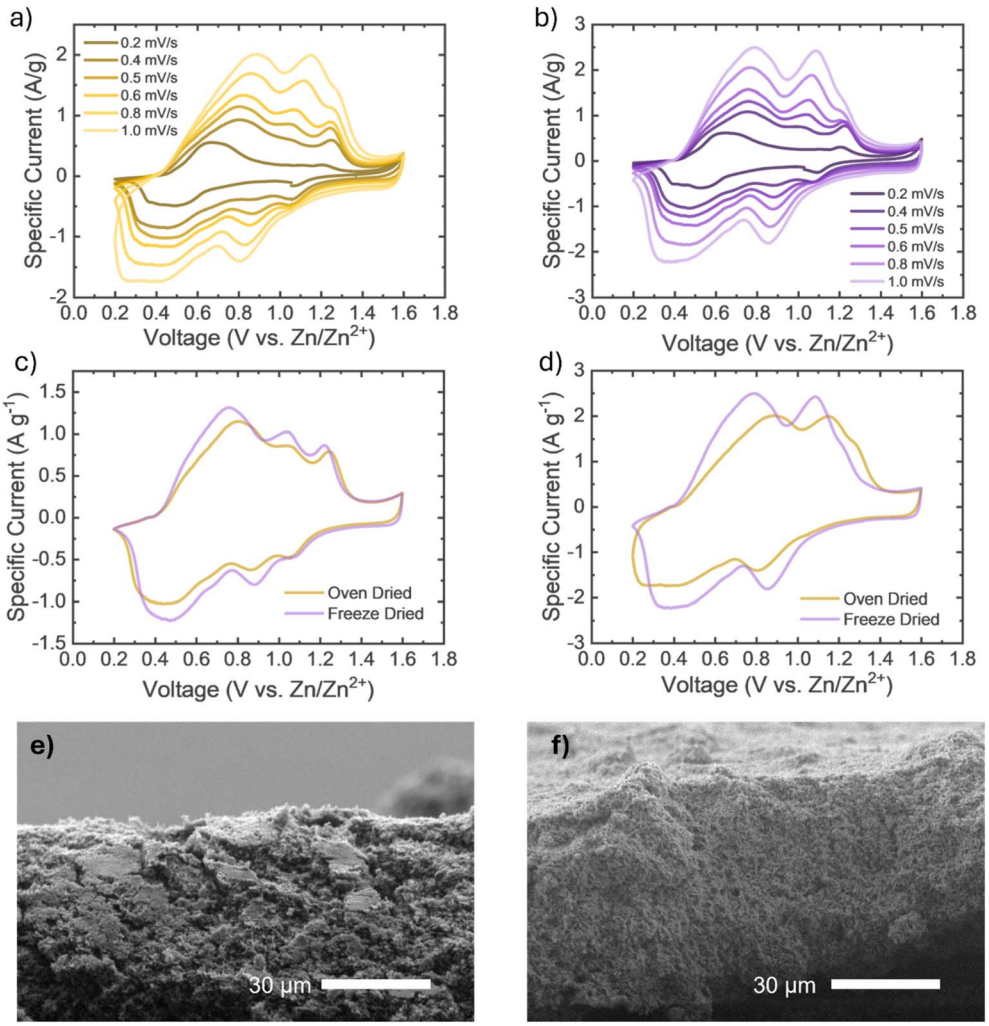

Fig. 5 Full CV curves of high mass cathodes dried by (a) vacuum oven and (b) freeze dryer. Comparative CV curves of drying methods at a scan rate of (c) 0.5 mV s^{-1} and (d) 1.0 mV s^{-1}. SEM images of VO_2(B) cathodes synthesised by (e) oven and (f) freeze drying.

a capacitive-controlled dominant process.[41] Fig. S5† displays the calculated *b* values for the peaks, which decreased as the mass loading of the cathode increased, indicating that the electrochemical process is moving from a capacitive-controlled process to a diffusion-controlled one. This is expected because the thickness of the cathode increases as the mass loading increases, thus requiring a greater diffusion of the ions. The *b* values in Table S1† also indicate that the freeze-dried cathode is more capacitive-controlled than the oven-dried one when comparing similar mass loading, which could be due to the increased porosity of the freeze-dried cathode and effective intercalation of ions. Lastly, the *b* values for the right-hand anodic peak (b) are always larger than that of the first (a). Similarly, the right-hand cathodic peak (c) has larger *b* values than the left cathodic peak (d). This means that the first intercalation step is more diffusive, as is the last deintercalation step. Initially, the ions need to overcome a higher diffusion barrier due to the initial structure of the electrode, nucleation and concentration limitations. The last deintercalation peak (d) also exhibits this as the Zn^{2+} ions are in low concentration. Thus, the diffusion path is increased as the remaining ions are embedded deeper within the cathode structure, structural changes occur, and polarisation further slows the ion transport.[43,44] The cross-sectional SEM images (Fig. 5e and f) of the cathodes show that the freeze drying process has increased the porosity of the cathode material. High magnification SEM images were also obtained (as seen in Fig. S6†), corroborating that the freeze-drying process has produced a more porous material. Conversely, the oven-dried sample has numerous relatively large clusters of VO_2(B), which reduces the surface area. There are many observed pores, which are all relatively uniformly formed – this could justify why the freeze-dried cathode cells perform better (larger surface area for ion movement).

Electrochemical impedance spectroscopy measurements were performed to determine the internal resistance of the cell

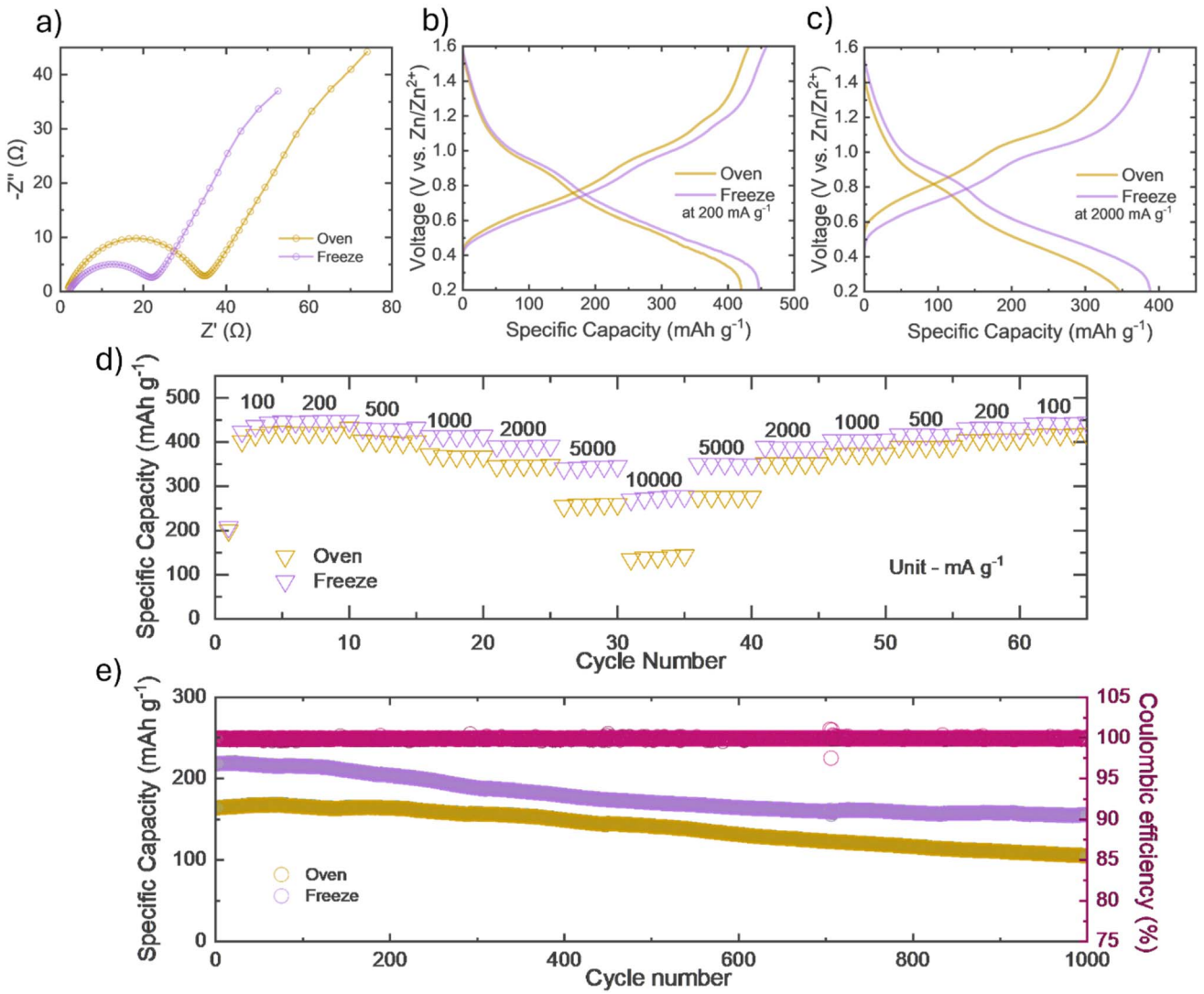

Fig. 6 (a) Nyquist plot of AZIBs with oven and freeze-dried cathodes with high mass loading. Comparative GCD curves of high mass loading cathodes, comparing drying methods at a specific current of (b) 200 mA g^{-1} and (c) 200 mA g^{-1}. (d) Rate test comparison of high mass, oven and freeze dried VO_2(B) cathodes. Long-term cycling of AZIBs with cathodes dried by different methods at (e) 2000 mA g^{-1}.

when assembled with differently dried cathodes. Fig. 6a displays the Nyquist plots of AZIBs with oven- and freeze-dried cathodes with a high mass loading. The cells have a relatively similar equivalent series resistance (ESR), as the first values on the *x*-axis are very similar. This means that there is similar total resistance, resulting in similar response times.[18,40,41] As the charge transfer resistance is lower in the oven-dried sample compared to the vacuum-dried one, it suggests that the redox reaction occurring at the cathode is quicker in the vacuum-dried sample compared to that of the oven-dried electrodes.[45]

Moreover, the GCD curves were obtained, alongside rate capacity plots, to analyse the specific capacity of the cells. Fig. 6b–d show that for both drying methods of the cathode with a high mass loading, high capacities of 447 mA h g^{-1} and 421 mA h g^{-1} were obtained for the freeze- and oven-dried cells, respectively, at 200 mA g^{-1}, which dropped to 388 mA h g^{-1} and 347 mA h g^{-1} at 2000 mA g^{-1}. It can be observed that at relatively lower specific

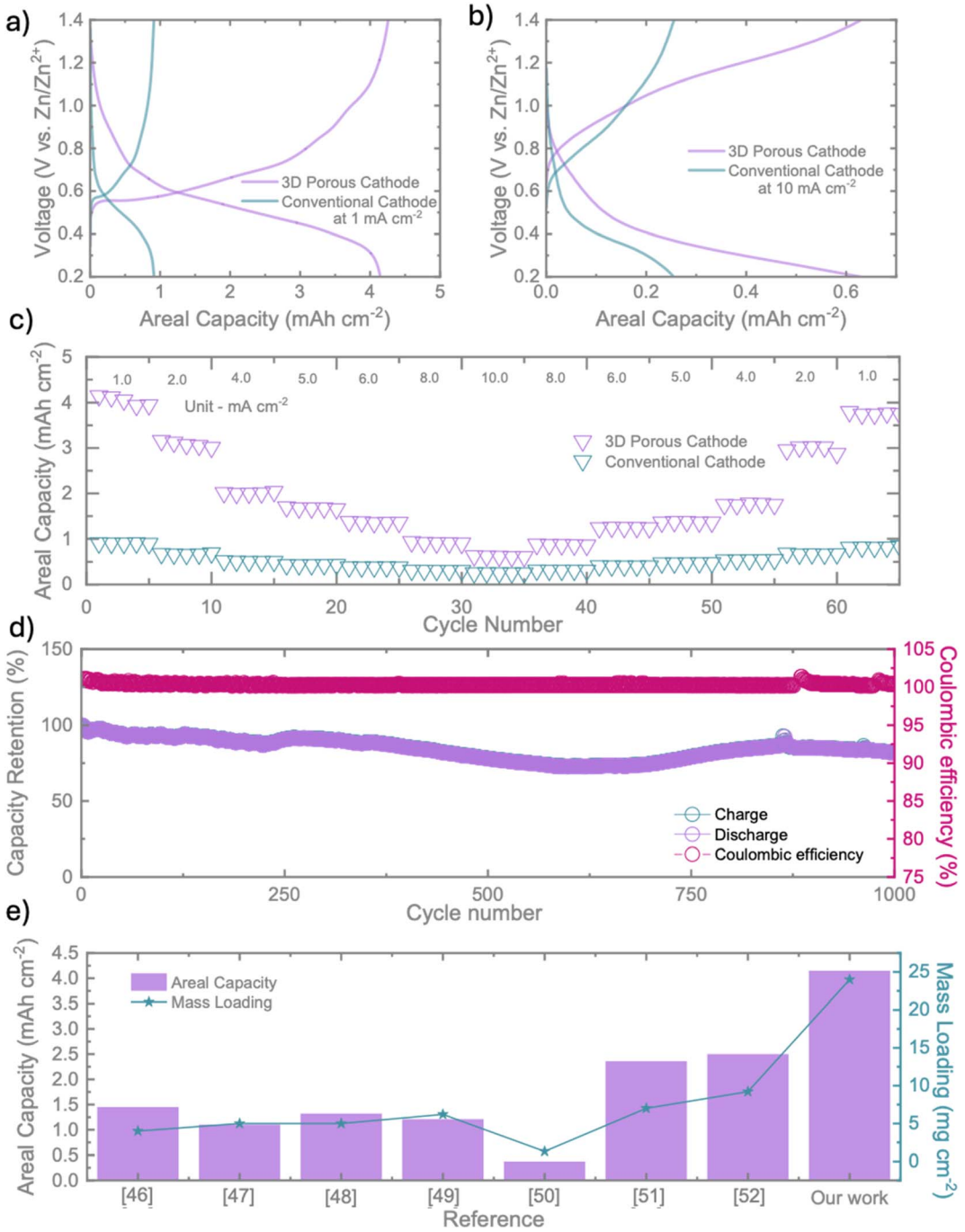

Fig. 7 Comparative GCD curves of 3D and conventional cathode cells with the applied areal currents of (a) 1 mA cm^{-2} and (b) 10 mA cm^{-2}. (c) Rate test comparison of cathodes at different applied areal currents. (d) Long-term cycling capacity retention of AZIB with a 3D cathode. (e) Comparison of areal capacities at an applied current of 1 mA cm^2 of this work with currently reported results.[46–52]

currents, the difference in capacities between the freeze-dried and oven-dried electrodes is minimal. However, at higher specific currents (*e.g.*, 10 000 mA g^{-1}), the freeze-dried electrodes exhibit significantly higher specific capacitance (276.8 mA h g^{-1}) compared to the oven-dried electrodes (143.5 mA h g^{-1}). This suggested that the drying method directly affects the cell performance, as expected. Thus, the freeze-drying process is more effective for achieving rate capability in batteries, while also offering higher capacity at relatively higher mass loading (Fig. 6d). Fig. 6e illustrates the long-term cycling performance of the electrodes, showing that freeze-dried electrodes maintained higher specific capacities compared to oven-dried electrodes. After 1000 cycles, the specific capacities measured are 155.8 mA h g^{-1} for freeze-dried electrodes and 105.7 mA h g^{-1} for oven-dried electrodes, with capacity retentions of 71.3% and 64.4%, respectively. Better capacities were observed in the freeze-dried electrode cells than the oven-dried cell when the applied specific current is increased. This could be due to the increased surface area of the freeze-dried cathode, allowing for greater (de) intercalation of ions in the same period of time (when comparing to 1000 mA g^{-1}). Thus, this supports the porosity theory of the freeze-dried cathode overcoming the limited depth penetration issue of ultrathick cathodes.

Ultrathick electrodes

The comparison of drying methods consolidated the theory that the porosity of the cathode is directly related to the improvement of the cell's performance in relation to high mass loading, as the freeze-dried cathodes have increased porosity. This theory was then applied to ultrathick cathodes (2.55 mm, as seen in Fig. S7†) with ultra-high mass loading (~24 mg cm^{-2}), which were based on carbon paper and a porous vitreous carbon foam (the porosity was expected to increase the surface area, similar to the working principle of the freeze-drying method). First, we performed cyclic voltammetry (CV) on the ultra-thick cathodes, as shown in Fig. S8a and b,† which demonstrated distinct redox peaks as expected. Fig. S8c† displays the GCD curves of the ultra-thick cathodes at different areal currents. Notably, the ultra-thick 3D cathode exhibits impressive charge storage performance, with significantly higher areal capacities compared to the conventional cathode. The measured areal capacitances are 4.15 mA h cm^{-2} and 0.63 mA h cm^{-2} at areal currents of 1 mA cm^{-2} and 10 mA cm^{-2}, respectively, which drop to 0.91 mA h cm^{-2} and 0.21 mA h cm^{-2} for conventional cathodes (Fig. 7a and b). The rate tests (Fig. 7c) further confirmed the impressive charge storage performance of our ultra-thick 3D cathodes compared to the conventional cathode. Moreover, long-term cycling tests revealed that the cell with the 3D cathode remained stable for 1000 cycles, retaining 81.7% capacity (Fig. 7d), consolidating the structural and electrochemical stability of the 3D cathodes as expected. The porous vitreous carbon foam structure clearly enhanced the mechanical stability of the cell, which was further improved by enclosing the cathode with two acrylic rings (each with a thickness of 0.8 mm) to maintain its mechanical structure, as seen in Fig. S7a and b.†

Finally, we compared the performance of our ultra-thick cathodes with those reported in the literature (as shown in Fig. 7e).[46–52] The most similar works still exhibited inferior performances in comparison to our work. Zhang, H. *et al.*[49] fabricated a cathode made of oxygen-deficient $ZnMn_2O_4$ with a mass loading of 6.2 mg cm^{-2}, yielding an areal capacity of 1.21 mA h cm^{-2}. Fang, K. *et al.*[51] developed a high mass-loading, binder-free, flexible vanadium oxide cathode with a mass loading of ~7 mg cm^{-2} and an areal capacity of 2.36 mg cm^{-2}. Lastly, Yang, H. *et al.*[52] reported on 3D printed carbon microlattices, over which MnO_2 was deposited to create the cathode for the ZIB. With a mass loading of 9.2 mg cm^{-2}, they obtained an areal capacity of 2.5 mA cm^{-2} for their microlattice system (all capacities were obtained at an applied current of 1 mA cm^{-2}). In our work, the mass loading was increased significantly, and the effect can be seen. No other work obtained an areal capacity similar to that which we have produced. This consolidates the theory that increased mass loading of the active material increases the surface area, and in turn, the number of sites for charge storage processes, thus increasing the capacity yielded. This comparison clearly demonstrates that our approach yields higher charge storage performance than the reported values. This further confirms that our synthesis and processing methods for materials and electrodes play a significant role in enhancing the overall charge storage performance.

Conclusion

Herein, we report a step-by-step investigation of material synthesis methods, electrode processing, and the fabrication of 3D cathodes. Our findings suggest that the hydrothermal synthesis of VO_2(B) cathodes results in superior charge storage performance. This enhancement is attributed to the formed morphology, increased oxygen vacancies, and a greater concentration of V^{4+} in the hydrothermal samples, which may facilitate more efficient Zn^{2+} ion intercalation compared to samples from the multiwave reactor. Electrochemical tests further confirm that freeze-dried cathodes demonstrate improved performance, owing to their larger surface area that promotes enhanced ion (de)intercalation and mobility, leading to faster charge transfer rates. The mass loading of the active material is a critical factor in cell performance; initially, as mass loading increases, cell performance improves. However, beyond a certain point, excessive mass loading leads to performance degradation. This is likely due to crack formation during the cathode drying process, limited ion penetration depth, and reduced overall conductivity of the electrodes. Introducing a 3D porous cathode offers a promising solution, as its large surface area prevents excessive slurry build-up, improves ion penetration, and results in higher areal capacities.

Data availability

All scientific data have been reported in the main manuscript and ESI.† The raw data files are available upon request from the corresponding authors.

Conflicts of interest

There are no conflicts to declare.

References

1 W. Du, E. H. Ang, Y. Yang, Y. Zhang, M. Ye and C. C. Li, *Energy Environ. Sci.*, 2020, **13**, 3330–3360.
2 L. Chen, Q. An and L. Mai, *Adv. Mater. Interfaces*, 2019, **6**, 1900387.
3 J. Ming, J. Guo, C. Xia, W. Wang and H. N. Alshareef, *Mater. Sci. Eng. R Rep.*, 2019, **135**, 58–84.
4 G. Fang, J. Zhou, A. Pan and S. Liang, *ACS Energy Lett.*, 2018, **3**, 2480–2501.
5 C. Li, X. Zhang, W. He, G. Xu and R. Sun, *J. Power Sources*, 2020, **449**, 227596.
6 M. Zhang, R. Liang, T. Or, Y.-P. Deng, A. Yu and Z. Chen, *Small Struct.*, 2021, **2**, 2000064.
7 R. K. Guduru and J. C. Icaza, *Nanomater.*, 2016, **6**, 41.
8 W. Bi, J. Chai, L. Meng, Z. Li, T. Xiong, J. Shu, X. Yao and Z. Peng, *ACS Appl. Mater. Interfaces*, 2023, **15**, 25594–25603.
9 J. R. Loh, J. Xue and W. S. V. Lee, *Small Methods*, 2023, **7**, 2300101.
10 T. Mageto, S. D. Bhoyate, K. Mensah-Darkwa, A. Kumar and R. K. Gupta, *J. Energy Storage*, 2023, **70**, 108081.
11 B. Tang, L. Shan, S. Liang and J. Zhou, *Energy Environ. Sci.*, 2019, **12**, 3288–3304.
12 T. Zhou, L. Zhu, L. Xie, Q. Han, X. Yang, L. Chen, G. Wang and X. Cao, *J. Colloid Interface Sci.*, 2022, **605**, 828–850.
13 T. R. Juran, J. Young and M. Smeu, *J. Phys. Chem. C*, 2018, **122**, 8788–8795.
14 Q. Zhao, W. Huang, Z. Luo, L. Liu, Y. Lu, Y. Li, L. Li, J. Hu, H. Ma and J. Chen, *Sci. Adv.*, 2018, **4**, eaao176.
15 M. Song, H. Tan, D. Chao, H. Jin Fan, M. Song, H. Tan, D. Chao and H. J. Fan, *Adv. Funct. Mater.*, 2018, **28**, 1802564.
16 T. Wei, Q. Li, G. Yang and C. Wang, *J. Mater. Chem. A*, 2018, **6**, 8006–8012.
17 B. Tang, J. Zhou, G. Fang, S. Guo, X. Guo, L. Shan, Y. Tang and S. Liang, *J. Electrochem. Soc.*, 2019, **166**, A480–A486.
18 J. Ding, Z. Du, L. Gu, B. Li, L. Wang, S. Wang, Y. Gong and S. Yang, *Adv. Mater.*, 2018, **30**, 1800762.
19 *MDI Materials Data*, 2019, preprint, Pro.
20 B. R. An, G. D. Lee, D. H. Son, S. H. Lee and S. S. Park, *Appl. Chem. Eng.*, 2013, **24**, 611–615.
21 C. Londoño Calderón, C. Vargas hernandez and J. Jurado, *Rev. Mex. Fis.*, 2010, **56**, 411–415.
22 B. Deka Boruah, A. Mathieson, S. K. Park, X. Zhang, B. Wen, L. Tan, A. Boies and M. De Volder, *Adv. Energy Mater.*, 2021, **11**, 2100115.
23 S. Milošević, I. Stojković, S. Kurko, J. G. Novaković and N. Cvjetićanin, *Ceram. Int.*, 2012, **38**, 2313–2317.
24 H. F. Xu, Y. Liu, N. Wei and S. W. Jin, *Optik*, 2014, **125**, 6078–6081.
25 J. Chen, B. Xiao, C. Hu, H. Chen, J. Huang, D. Yan and S. Peng, *ACS Appl. Mater. Interfaces*, 2022, **14**, 28760–28768.
26 J. C. Valmalette and J. R. Gavarri, *Mater. Sci. Eng. B*, 1998, **54**, 168–173.
27 H. Ji, D. Liu, H. Cheng, C. Zhang, L. Yang and D. Ren, *RSC Adv.*, 2017, **7**, 5189–5194.
28 N. Wang, Y. Zhang, T. Hu, Y. Zhao and C. Meng, *Curr. Appl. Phys.*, 2015, **15**, 493–498.
29 M. C. Biesinger, L. W. M. Lau, A. R. Gerson and R. S. C. Smart, *Appl. Surf. Sci.*, 2010, **257**, 887–898.
30 Y. Fu, Y. Liu, K. Ma, Z. Ji, W. Mai and C. Zhao, *J. Alloys Compd.*, 2020, **819**, 153063.
31 M. J. Powell, I. J. Godfrey, R. Quesada-Cabrera, D. Malarde, D. Teixeira, H. Emerich, R. G. Palgrave, C. J. Carmalt, I. P. Parkin and G. Sankar, *J. Phys. Chem. C*, 2017, **121**, 20345–20352.
32 P. M. V. Raja and A. R. Barron, BET surface area analysis of nanoparticles, **https://chem.libretexts.org/Bookshelves/Analytical_Chemistry/Physical_Methods_in_Chemistry_and_Nano_Science_(Barron)/02%3A_Physical_and_Thermal_Analysis/2.03%3A_BET_Surface_Area_Analysis_of_Nanoparticles**, accessed 11 May 2024.
33 N. Wang, Y. Zhang, T. Hu, Y. Zhao and C. Meng, *Curr. Appl. Phys.*, 2015, **15**, 493–498.
34 Z. Li, S. Ganapathy, Y. Xu, Z. Zhou, M. Sarilar, M. Wagemaker, Z. Li, S. Ganapathy, Y. Xu, Z. Zhou, M. Sarilar and M. Wagemaker, *Adv. Energy Mater.*, 2019, **9**, 1900237.
35 L. Chen, Y. Ruan, G. Zhang, Q. Wei, Y. Jiang, T. Xiong, P. He, W. Yang, M. Yan, Q. An and L. Mai, *Chem. Mater.*, 2019, **31**, 699–706.
36 B. Zhang, J. Chen, W. Sun, Y. Shao, L. Zhang and K. Zhao, *Energies*, 2022, **15**, 4698.
37 P. Shvets, O. Dikaya, K. Maksimova and A. Goikhman, *J. Raman Spectrosc.*, 2019, **50**, 1226–1244.
38 A. Bafaqeer, M. Tahir and N. A. S. Amin, *Appl. Surf. Sci.*, 2018, **435**, 953–962.
39 D. Louloudakis, D. Vernardou, E. Spanakis, M. Suchea, G. Kenanakis, M. Pemble, K. Savvakis, N. Katsarakis, E. Koudoumas and G. Kiriakidis, *Adv. Mater. Lett.*, 2016, **7**, 192–196.
40 K. Guan, K. Duan, G. Yang, L. Tao, H. Zhang, H. Wan, R. Yang, J. Zhang, H. Wang and H. Wang, *Mater. Today Adv.*, 2022, **14**, 100230.
41 V. Augustyn, J. Come, M. A. Lowe, J. W. Kim, P. L. Taberna, S. H. Tolbert, H. D. Abruña, P. Simon and B. Dunn, *Nat. Mater.*, 2013, **12**(6), 518–522.
42 B. K. Lesel, J. S. Ko, B. Dunn and S. H. Tolbert, *ACS Nano*, 2016, **10**, 7572–7581.
43 J. Gong, H. Li, K. Zhang, Z. Zhang, J. Cao, Z. Shao, C. Tang, S. Fu, Q. Wang and X. Wu, *Nanomaterials*, 2022, **12**, 1438.
44 C. Cai, Z. Tao, Y. Zhu, Y. Tan, A. Wang, H. Zhou and Y. Yang, *Nanoscale Adv.*, 2021, **3**, 3780–3787.
45 S. Roy, S. Marzorati, A. Schievano and D. Pant, *Encyclopedia of Sustainable Technologies*, 2017, pp. , pp. 245–259.
46 M. Zhao, Y. Luo, L. Zhu, D. Cai, Y. Zhuang, Q. Chen and H. Zhan, *J. Alloys Compd.*, 2022, **913**, 165124.
47 Y. Jiang, D. Ba, Y. Li and J. Liu, *Adv. Sci.*, 2020, **7**, 1902795.
48 F. Li, Y. L. Liu, G. G. Wang, D. Yan, G. Z. Li, H. X. Zhao, H. Y. Zhang and H. Y. Yang, *J. Mater. Chem. A*, 2021, **9**, 9675–9684.

49 H. Zhang, J. Wang, Q. Liu, W. He, Z. Lai, X. Zhang, M. Yu, Y. Tong and X. Lu, *Energy Storage Mater.*, 2019, **21**, 154–161.
50 J. Liu, C. Guan, C. Zhou, Z. Fan, Q. Ke, G. Zhang, C. Liu, J. J. Wang P Liu, C. Zhou, C. Guan, Z. Fan, Q. Q. Ke, J. Wang, G. Z. Zhang and C. Liu, *Adv. Mater.*, 2016, **28**, 8732–8739.
51 K. Fang, F. Li, G. G. Wang, Y. L. Liu, M. L. Tan, D. Q. Zhao, H. Y. Zhang and J. C. Han, *J. Mater. Sci. Technol.*, 2023, **143**, 84–92.
52 H. Yang, Y. Wan, K. Sun, M. Zhang, C. Wang, Z. He, Q. Li, N. Wang, Y. Zhang, H. Hu and M. Wu, *Adv. Funct. Mater.*, 2023, **33**, 2215076.